Nanoscale

Flagellar nanorobot with kinetic behavior investigation and 3D motion

Journal:	*Nanoscale*
Manuscript ID	NR-ART-03-2020-002496.R1
Article Type:	Paper
Date Submitted by the Author:	18-May-2020
Complete List of Authors:	Tang, Jiannan; Southern Methodist University Rogowski, Louis; Southern Methodist University, Department of Mechanical Engineering Zhang, Xiao; Southern Methodist University Kim, Min Jun; Southern Methodist University, Department of Mechanical Engineering

ARTICLE

Flagellar nanorobot with kinetic behavior investigation and 3D motion

Received 00th January 20xx,
Accepted 00th January 20xx

DOI: 10.1039/x0xx00000x

Jiannan Tang, Louis William Rogowski, Xiao Zhang, and Min Jun Kim*

Wirelessly controlled nanorobots have the potential to perform highly precise maneuvers within complex *in vitro* and *in vivo* environments. Flagellar nanorobots will be useful in a variety of biomedical applications, however, to date there has been little effort to investigate essential kinetic behavior changes related to the geometric properties of the nanorobot and effects imparted to it by nearby boundaries. Flagellar nanorobots are composed of an avidin-coated magnetic nanoparticle head (MH) and a single biotin-tipped repolymerized flagellum that are driven by a wirelessly generated rotating magnetic field. Nanorobots with different MHs and flagellar lengths were manually guided to perform complex swimming trajectories under both bright-field and fluorescence microscopy visualizations. The experimental results show that rotational frequency, handedness of rotation direction, MH size, flagellar length, and distance to the bottom boundary significantly affect the kinematics of the nanorobot. The results reported herein summarize fundamental research that will be used for the design specifications nessecssary for optimizing the application of helical nanorobotic devices for use in delivery of therapeutic and imaging agents. Additionally, robotic nanoswimmers were sucessfully navigated and tracked in 3D using quantitative defocusing, which will significantly improve the efficiency, function, and application of flagellar nanorobot.

Introduction

Small-scale robots have the potential to perform a wide range of biomedical applications due to their ability to navigate within cellular and sub-cellular working spaces. While small-scale robots have been shown to perform drug delivery[1-3], microscale transport[4, 5], enhanced convection[6], *in vivo* imaging[7, 8], and *in vitro* cell manipulation[9], there are still numerous challenges that need to be overcome[10] where processes, such as power sourcing, precise actuation, multifunctional integration, drug payload attachment, and their precise deployment mechanisms, are still being refined. Some strategies have already been developed to achieve nanorobot navigation, including the application of externally applied forces (*e.g.* magnetic[11], electric[12], ultrasound [13], and light [14]), biological motors[15], and chemical fuels[16]. At low Reynolds numbers (Re << 1), viscous forces have a greater effect on propulsion since inertial forces are considered nonexistent, thus microswimmers are required to have specialized swimming geometries[17]. Microscale swimming methods have been developed to mimic microorganisms like prokaryotes and eukaryotes[18], where swimming with a helical propeller, swimming with an elastic tail, and pulling through the fluid medium with self-produced field gradients are the three most common microorganism propulsion methods[19]. Among these three swimming methods the helical propeller is the best overall choice for *in vivo* applications[20] due to its ubiquity at the small-scale and high torque potential. Since helical propellers have a lot of potential research values such as mechanical mapping, drug delivery, stirring/mixing at the subcellular level, and many other developing applications, it has attracted a great deal of interest within the scientific community and is worth exploring further here.

Fabricating a helical geometry to mimic those used by bacterial organisms has not been an easy task. The top-down fabrication methods presented in literature, such as the self-scrolling technique[21-23], 3-dimensional (3D) lithography[4, 24], biotemplate synthesis[8, 25, 26] and glancing angle deposition[27-29], have created viable artificial helical microswimmers. These microswimmers have since been used to achieve novel applications such as enhancing convection properties[6] and delivering microparticles[3] in 2-dimensional space (2D). However, these top-down fabrication methods often require a series of complex fabrication steps and necessitate extremely specialized equipment. Moreover, the artificial helical shaped flagella produced from these top-down techniques cannot replicate the unique structural properties inherent to protein assembled bacterial flagella; among which include their hollow structure (2 nm inner diameter, 20 nm outer diameter), the ability to polymorphically transform in response to external stimuli, and their structure consisting of naturally self-assembling nanotubular components called flagellin[30]. Flagella have also been documented to persevere in extreme pH environments (*e.g.* pH 3-11) and temperatures up to 60 ^{o}C[31]. Due to the unique advantages of the flagella, bacterial nanorobots were then shown to successfully propel in 2D using rotating magnetic fields. Through a combination of

Department of Mechanical Engineering, Lyle School of Engineering, Southern Methodist University, Dallas, TX 75275, U.S.A.
**Corresponding author. E-mail: mjkim@lyle.smu.edu*
Electronic Supplementary Information (ESI) available: [details of any supplementary information available should be included here]. See DOI: 10.1039/x0xx00000x

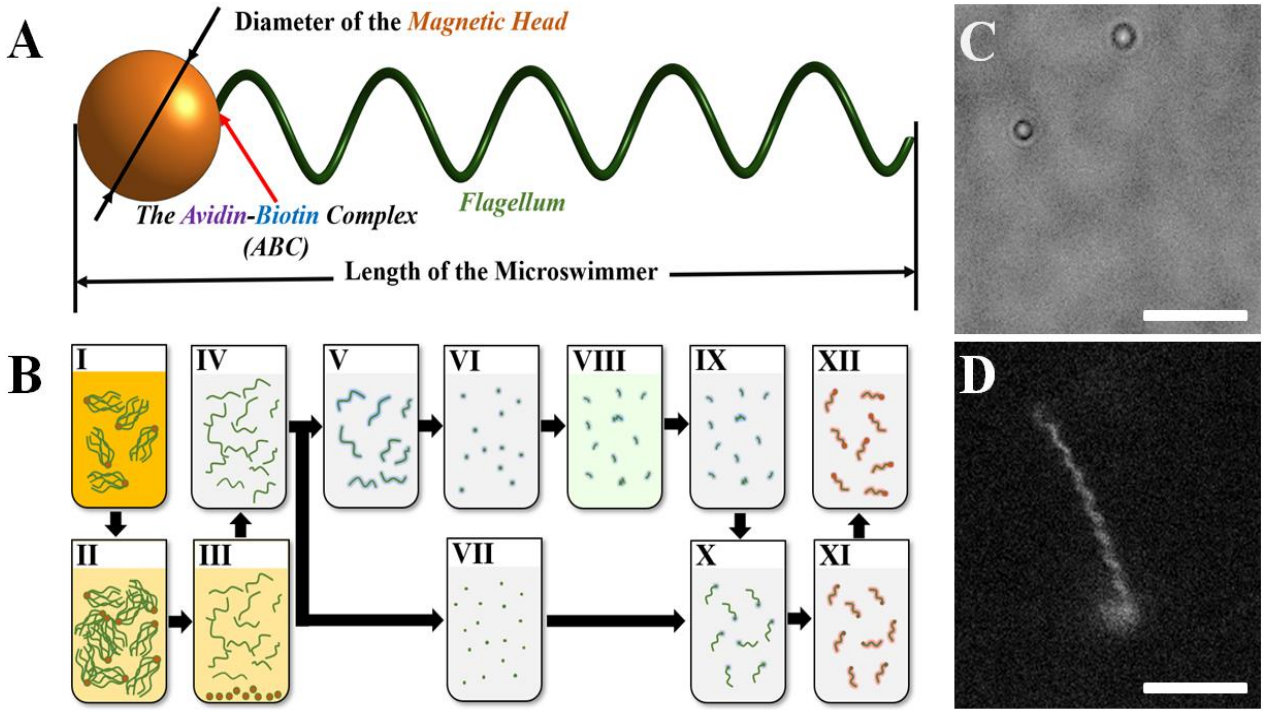

Figure 1. Fabrication of the flexible flagellar nanorobot. (A) Sketch of a flagellar nanorobot with a single magnetic nanoparticle. (B) The fabrication process of the flagellar nanorobot (more detail could be found in the Experimental section). (C) Flagellar nanorobot under bright-field microscopy visualization. (D) Flagellar nanorobot under fluorescence microscopy visualization. All scale bars are 10 μm.

experimental[11] and numerical research[32], the performance and behaviour of flagellar nanoswimmers were documented under coiled, curly and normal polymorphic forms, with the normal form being found to be the most efficient at swimming[11]. However, some physical effects influencing nanorobot propulsion have not been well investigated, with the size of the MH used in fabrication, the length of the attached flagella, proximity to sample chamber boundaries, and the effect of flagella handedness in relation to the rotation direction of the magnetic fields.

Additionally, to date there has been no work performed to manipulate helical nanoswimmers in 3D, which continues to remain a highly restrictive obstacle to the field of small-scale robotics in terms of both imaging and controls. In literature, 1 to 10 μm diameter sphere-shaped magnetic particle was positionally guided with a magnetic tweezer system[33, 34]; however, for the smaller particle, because of Brownian motion [35], uncertain velocity in random directions occurred and made the magnetic particle uncontrollable using the tweezer system [36]. Besides, nanorobots based on helices require a torque to meaningfully propel, thus the tweezer system, operated by a magnetic field gradient, is not suitable. Three typical magnetic field control systems, Helmholtz, OctoMag, and MiniMag, were investigated by Schuerle et al.[37]. Compared with others listed, the MiniMag was found to have fewer physical restrictions to the workspace and it has the ability to enable different magnetic micromanipulation methods, useful to targeted drug delivery and single-cell manipulation. To simulate the rotary motor of bacterial flagella in our experiments[38] and generate the propulsion in 3D, a rotating magnetic field was applied. In terms of imaging and tracking a nanorobot in 3D, several researchers have proposed different methods to address this; Daluglu et al.[39-41] proposed a computational imaging technique that could measure microswimmers in 3D, with the help of two LEDs and complementary metal-oxide-semiconductor image sensor; however imaging setup requires specialized equipment and is not accessible in most real world applications. Besides, the maneuverable and cheaper alternative known as quantitative defocusing method has previously been applied to track the 3D trajectory of microparticles[42].

Combing the flagellar nanorobot with the 3D tracking method, in this paper, we report the kinetic behavior of flagellar nanorobots with normal polymorphic forms under the actuation a magnetic field generator; the magnetic field generator (MFG-100, MagnebotiX) was similar to the MiniMag used in other work[43]. The quantitative defocusing method was used to track the flagellar nanorobots position in 3D space. The kinetic behavior observed by the nanorobots brought up several novel properties that have not been addressed in literature, including critical factors like the nanorobots distance from the substrate, the length of the nanorobot, size of the MH, rotating frequency, and the handedness of rotating direction; all of which were found to significantly affect nanorobot performance. Furthermore, we present the first time a

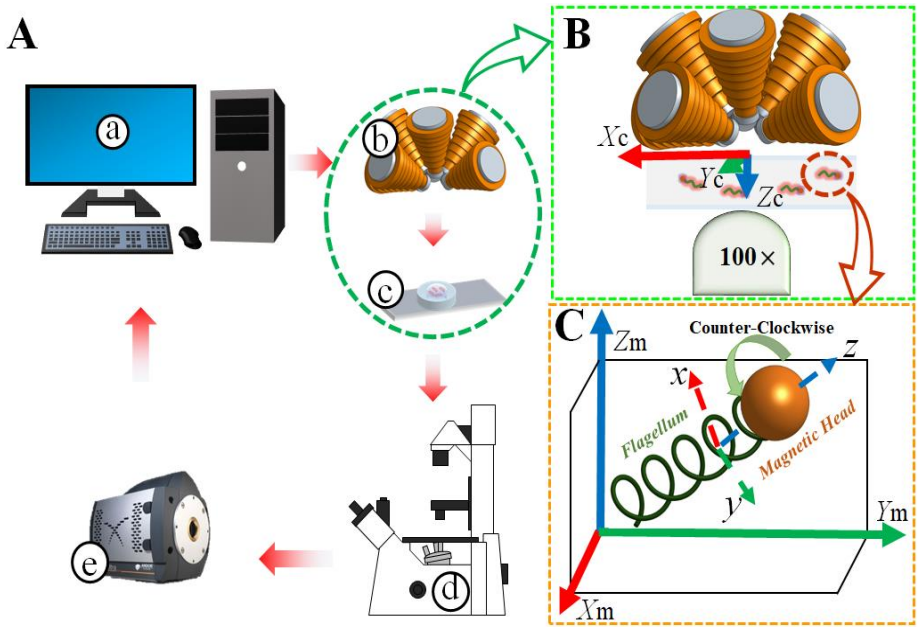

Figure 2. Overview of the imaging and control systems and coordinates. (A) Overview of the imaging and the magnetic control system. (a) Magnetic field control program (Daedalus) and imaging program (NIS-Element AR) are operated on a computer. (b) Power supply (ECB-820) and Magnetic field generator (MFG-100, MagnebotiX). (c) Nanorobot suspended inside a PDMS sample chamber. (d) The inverted fluorescence microscope (Nikon Eclipse Ti). (e) EMCCD camera (iXon 897, Andor Technology, resolution 512×512). (a) and (b) formed the magnetic control system, and (a), (d) and (e) formed the imaging system (Figure S2). (B) Diagram of the magnetic field generation system in the experiment, where $X_cY_cZ_c$ is the magnetic control system general Cartesian. (C) Schematic of the rotating magnetic field, where the $X_mY_mZ_m$ and xyz are the microscope system general Cartesian coordinate and the local Cartesian coordinate of the flagellar nanorobot respectively.

nanorobot was successfully tracked in 3D to perform user-selected trajectories. The results presented here will eventually be used to help benefit the robotics and fluid dynamics communities by providing a reference that characterizes the generalized performance behavior of flagellar nanorobots under varying geometric and actuation parameters.

Results and discussion

Flagellar nanorobot fabrication

The flagellar nanorobots used during experiments consist of both a magnetic nanoparticle and a flagellum (of variable length) that are bonded together using an avidin-biotin complex (Figure 1A). The flagellum had their endpoints coated with biotin using a sequential repolymerization process, and the nanoparticle was prefabricated with an avidin surface coating (Spherotech, SVM-025-5H). The total diameter of the nanoparticle (single or aggregated) attached to the flagellar endpoints will be referred to as the 'magnetic head (MH)', and will be used as a substitute for MH diameter.

Flagella [44] were harvested from *Salmonella typhimurium* (SJW1103) and repolymerized using a modified version of Asakura's method[45, 46]. Figure 1B illustrates an overview of the fabrication process of the flagellar nanorobot, with the full details discussed in the Experimental section. After harvesting the flagella from the bacteria and purifying it from the culture media (I, II, III, and IV of Figure 1B), a small portion of the concentrated flagella was biotinylated, depolymerized, and salted-out to form seeding particles (V, VI, VIII and IX of Figure 1B). The rest of the concentrated flagella was thermally depolymerized and mixed with the biotinylated seeding particles for repolymerization (VII and X of Figure 1B); after labeling (Cy3, GE Healthcare, PA23001) the flagella and mixing them with avidin magnetic particles, the flagellar nanorobots naturally self-assembled together. (XI and XII of Figure 1B). While many variants of flagellated nanorobots form during this process, only nanorobots with a single flagellum were investigated within this paper.

An inverted fluorescence microscope (Nikon Eclipse Ti) and electron-multiplying charge-coupled device (EMCCD) camera (iXon 897, Andor Technology) were used to visualize the flagellated nanorobot suspended in a conjugation buffer solution under both bright-field (Figure 1C) and fluorescence microscopy (Figure 1D). In the bright-field, only the MH could be clearly visualized, on the contrary, under the fluorescent field, the labeled flagella, including their geometrical characteristics (pitch, length, and coil form), could be apparently identified.

Controlling and imaging systems

The flagellar nanorobot (Movie S1) could be controlled by the magnetic field generating system (a and b of Figure 2A) and visualized by the imaging system (a, d, and e of Figure 2A) during experiments. The MH of the microswimmer will synchronously rotate with the rotating magnetic field where the resulting rotation drives the helical flagellum and induces a reactive force

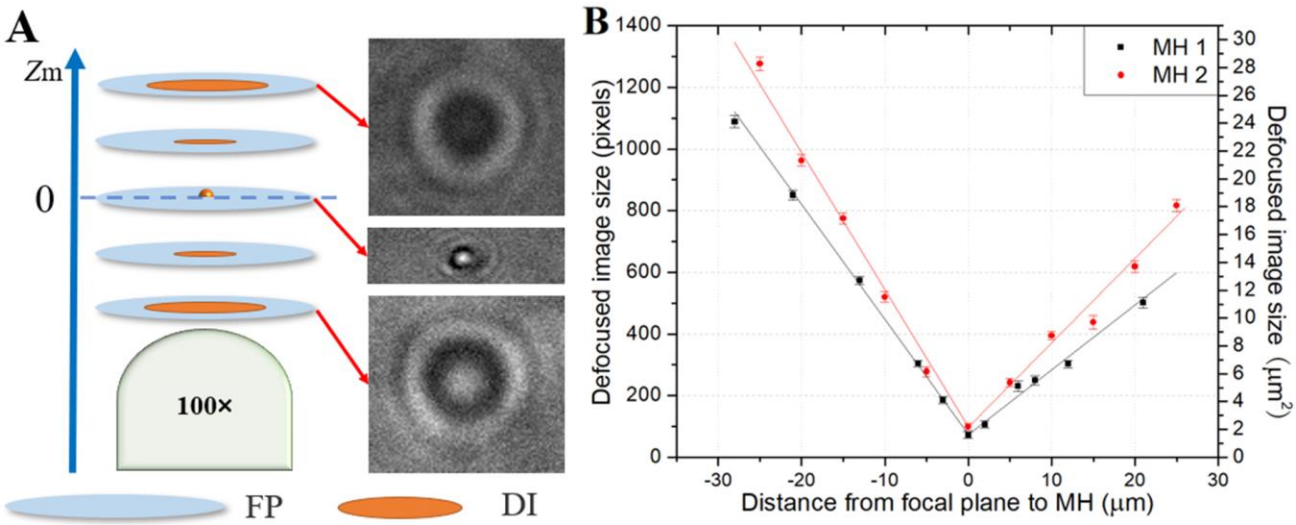

Figure 3. Overview of the Z_m-direction tracking algorithm. (A) Overview of the quantitative defocused method, where FP and DI are the abbreviation of the focal plane and defocused image, respectively. (B) Relationships between the distance of the focal plane to MH in the Z_m-direction and defocused image size. Lines between points were added to guide the eye.

with the liquid medium. This reactive force has two components, propulsion and equilibrant, which are along and perpendicular to axis, respectively. The equilibrant keeps the nanorobot propelling stably along its axis. At the same time, the propulsion will be greater then the resistance force at the beginning, and accelerate the flagellar nanorobot until the resistance increases with the velocity enough to balance the propulsion, and finally the flagellar nanorobot will swim with a constant velocity in the medium (Figure S1).

MATLAB was used to process imaging and video data, track the nanorobots under both bright-field and fluorescence microscopy visualizations, analyze nanorobot trajectory, velocity, geometrical characteristics (such as the length of the flagellum and the diameter of the MH), and create detailed plots. In this process, the measurment values of the area, length, and location of every connected component in the figures or videos were expressed by the number of pixels. Using a pixel distance conversion, the kinetic and geometrical characteristic of the flagellar nanorobots were converted to μm, μm /s, μm², etc.

Using the fluorescence microscopy (Figure 1D), the geometrical parameters such as the length, pitch, and the number of turns could be visually determined by inspection. However, the fluorescent field does not have the detection ability necessary to measure the imaging distance, which we define as the maximum Z_m direction distance (μm) from the focal plane to the nanorobot that can be visualized; because of this, tracking the trajectory of the nanorobot along Z_m-direction (Figure 2B) in the fluorescent field was extremely difficult. Using the bright-field (Figure 1C), only the MH of the nanorobot could be visualized clearly. For 2D tracking, the trajectory of the MH centroid in X_mY_m plane was recorded directly, and the quantitative defocusing method [42, 47] was used to determine the relationship between the distance away from the focal plane along Z_m-direction and the defocused MH size. Figure 3 illustrates the overview of the quantitative defocusing method and the relationships of two different sizes of MHs, which are 1.2 μm and 1.7 μm diameter respectively, through experimentation. In Figure 3A, the image size is at its minimum when the focal plane is located directly on the MH, and the defocused image size increases when the focal plane deviates from the original MH position. The defocused images of two MHs at different focal plane locations were photographed, and the size of all defocused images were extracted, recorded and shown as pixel values in MATLAB (Figure S3 and size measurement in SI). Figure 3B shows the relationship between the distance of the focal plane to the MH in Z_m-direction and defocused image size, which are almost linear before and after the MH's zeroth focal plane (both the number of pixels and area in μm² are shown on the axes). Also, the slopes of the MH area's are different depending on the positive and negative signs of the distance from the zeroth focal plane.

For the data presented here, the geometric morphologies and the 2D trajectories of nanorobots were recognized in the fluorescent field, whilethe 3D trajectories of nanorobots were investigated in the bright-field only after obtaining the relationship between the Z_m-direction distance (μm) and defocused image size (pixels and μm²) of the MH in relation to the graph shown in Figure 3B.

The influence from the substrate boundary

The influences from the boundary on helical nanorobot's performance have not been investigated deeply[11, 27, 32]. In realistic scenarios for drug delivery, nanorobots will need to work in complicated *in vitro* and *in vivo* environments, such as HEC hydrogels and pulmonary mucus, which have narrow and confined porous structures[48]. Therefore, understanding the influence of the boundary is critical for understanding the motion characteristics of nanorobots (Movie S2). To investigate

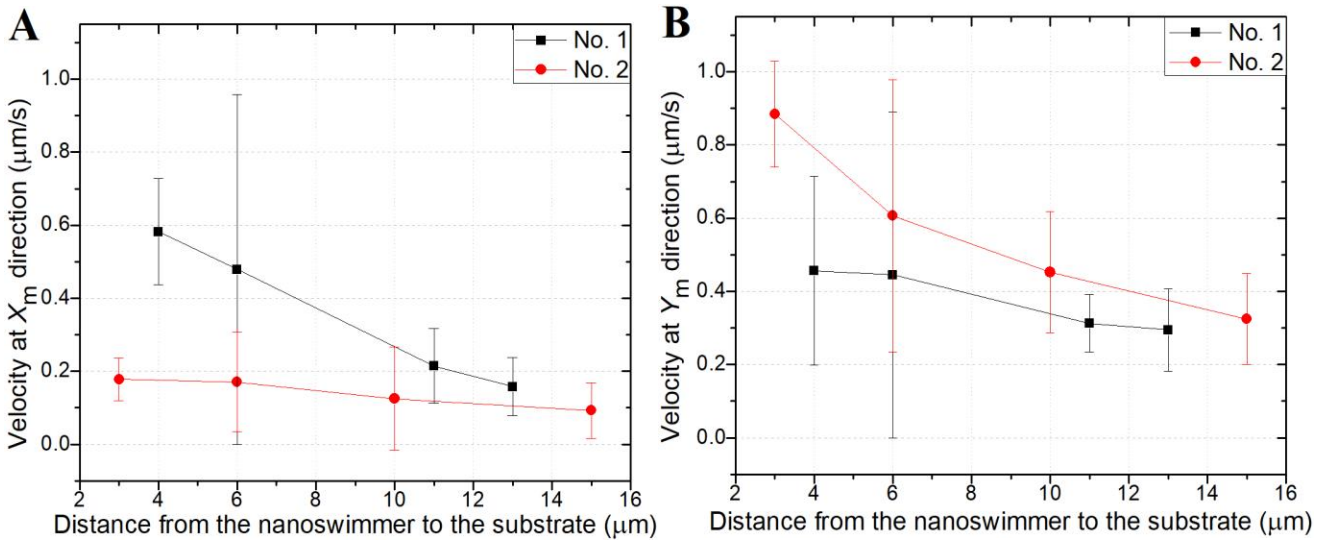

Figure 4. Velocities of the No.1 (6 μm long, 0.82 μm diameter of MH at 5 Hz) and No. 2 (6 μm long, 0.27 μm diameter of MH at 5 Hz) at different distances between the nanorobot and the bottom-substrate. (A) Velocities of the No.1 and No. 2 nanorobots at X_m direction. (B) Velocities of the No.1 and No. 2 nanorobots at Y_m direction. Lines between points were added to guide the eye.

the boundary effect, particularly from the substrate at the bottom of the sample chamber, two nanorobots, No. 1 (6 μm long with a MH size of 0.82 μm) and No.2 (6 μm long with a MH of 0.29 μm diameter, which is a single magnetic particle), were controlled by a 5 Hz rotating magnetic field, which rotated about the Y_m direction that coincided with the nanorobots swimming direction. After the locations of the substrate and nanorobot in the Z_m direction were obtained, the distance between the nanorobot and substrate was determined through subtraction. As the nanorobot swims in Z_m direction, the effect substrate proximity has on the velocities along the X_m and Y_m direction were determined and plotted in Figure 4A and B respectively. Figure 4A shows that helical nanorobots not only moved forward along the Y_m direction but also moved laterally along X_m direction, which is perpendicular to the rotation axis of the nanorobot, due to the rotating shear force induced flow fields interacting with the boundary. The X_m direction velocity increased as the nanorobot approached the substrate. The different sizes of the MH greatly influenced the perpendicular X_m direction velocities, as the No. 1 nanorobot (larger MH) sharply decreased as the distance from the substrate increased, in stark contrast to the results of the No. 2 nanorobot (smaller MH). Additionally, based on the results in Figure 4B, the swimming velocities (Y_m direction) of the two nanorobots decreased while the distance from the substrate increased.

Overall, these results indicate that boundary effects can heavily influence nanorobot velocities along the rotation axis and lateral direction. Proximity to the substrate caused higher velocity for both directions, particularly when the distance was less than 20 μm, the lateral velocity increased significantly. The

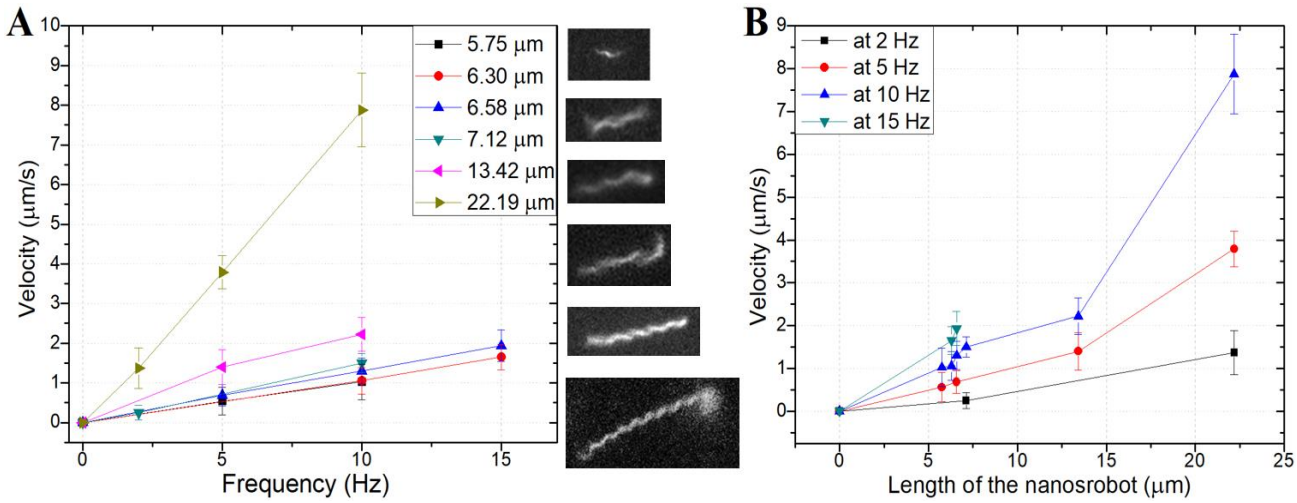

Figure 5. (A) Velocity of nanorobots at different magnetic field rotation frequencies. (B) Velocity of nanorobots with different lengths of flagella. Lines between points were added to guide the eye.

larger MH size also resulted in a larger lateral velocity when compared to the velocity along the rotating axis. This relationship could be potentially used to detect hidden surroundings in the fluid as the nanorobots propel and its velocity profiles change; this would be useful in biological fluids where heterogeneities tend to disrupt normal propulsion mechanisms. To verify this, subsequent experiments were done where the distance between the nanorobot and bottom substrate was larger than 20 μm and as a result no obvious lateral velocity was produced by the nanorobot.

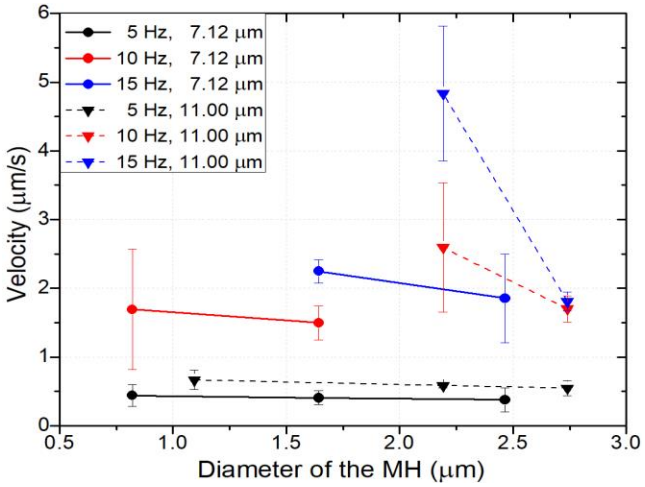

Figure 6. The velocity of nanorobots with different MH diameters and flagellum lengths at different frequencies. Lines between points were added to guide the eye.

The effect of flagellar nanorobot geometric parameters

To determine the swimming effectiveness of flagellar nanorobots under different rotating magnetic fields (Movie S3) and geometric compositions (Movie S4), experiments were systematically performed on nanorobots possessing different lengths of flagella and sizes of MH. These nanorobots were exposed to varying magnetic field rotation frequencies and rotation directions (clockwise and counter-clockwise when looking along the positive *z* axis of the nanorobots local coordinates, Movie S5) during experiments to analytically compare their performances.

To investigate the effect of the length of nanorobot on the swimming velocity and avoid the effect from the size of the MH, only nanorobots with the same size of MH (diameter is about ~270 nm) attached with a single flagellum were investigated. The velocity profiles of nanorobots at different rotational frequencies are shown in Figure 5.

Figure 5A presents the velocity of nanorobots with different lengths of attached flagellum. The results show that the velocities of all nanorobots observed tended to linearly increase as the rotating magnetic field's frequency increased. This linear relationship was verified previously by numerically simulated helical models[49, 50], where the magnetic rotating frequency could linearly control the nanorobots speed and nanorobots with longer flagellum were observed to swim faster at the same rotating frequency (Figure 5A). Furthermore, in order to obtain the relationship between the velocity and the length of the nanorobot, the results in Figure 5A were rearranged into Figure 5B which shows how flagellar length affects velocity. Different from the linear relationship between the velocity and rotational frequency seen previously (Figure 5A), the relationship between velocity and flagellar length appears to be nonlinear (Figure 5B). What is interesting in this data is that the length of the nanorobot affects velocity more than rotational frequency; this could be later optimized for *in vivo* situations where low torques are required.

To investigate the influence of the MH size on the velocity of nanorobots, three approximate 7.12±0.2 μm long

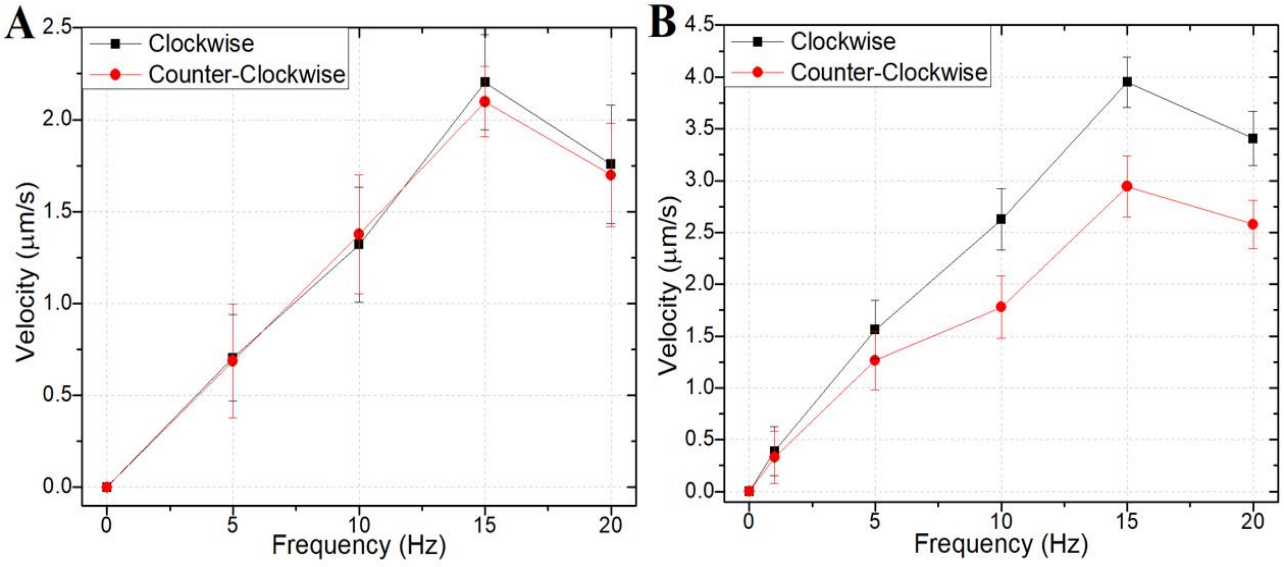

Figure 7. (A) The velocity of the nanorobots in the clockwise and counter-clockwise magnetic field (diameter of MH = 290 nm, length of the nanorobot = 9.58 μm). (B) The velocity of the nanorobots in the clockwise and counter-clockwise magnetic field (diameter of MH = 1000 nm, length of the nanorobot = 16.58 μm). Lines between points were added to guide the eye.

nanorobots with different sizes of MH were manipulated to swim at 5 Hz, 10 Hz and 15 Hz rotating magnetic fields. The results (solid line) in Figure 6 show as the MH increases, the velocity decreases at all rotating frequencies. Another group of three 11.00±0.2 μm long nanorobots with different sizes of MH were manipulated to undergo the same experiments and are shown as the dotted lines in Figure 6; these results confirm that increasing in MH size has a negative linear influence on the nanorobots swimming speed; we suspect that the larger cross-sectional area of MH generates more resistance (Stokes' Law, see SI).

Until now, all of the nanorobots shown were actuated with counter-clockwise rotating magnetic fields. In this section, two nanorobots with different sizes of MH were controlled to move forward (*z* direction in Figure 2C) and backward forward (-*z* direction in Figure 2C) under counter-clockwise and clockwise rotating magnetic fields at different rotating frequencies, respectively. The change in the rotation direction, depending on the coil form of the flagella, will usually create a reversal in the swimming direction[51]. Figure 7A shows that rotational direction does not significantly impact nanorobot swimming velocity with a 290 nm diameter MH. However, the velocities of the

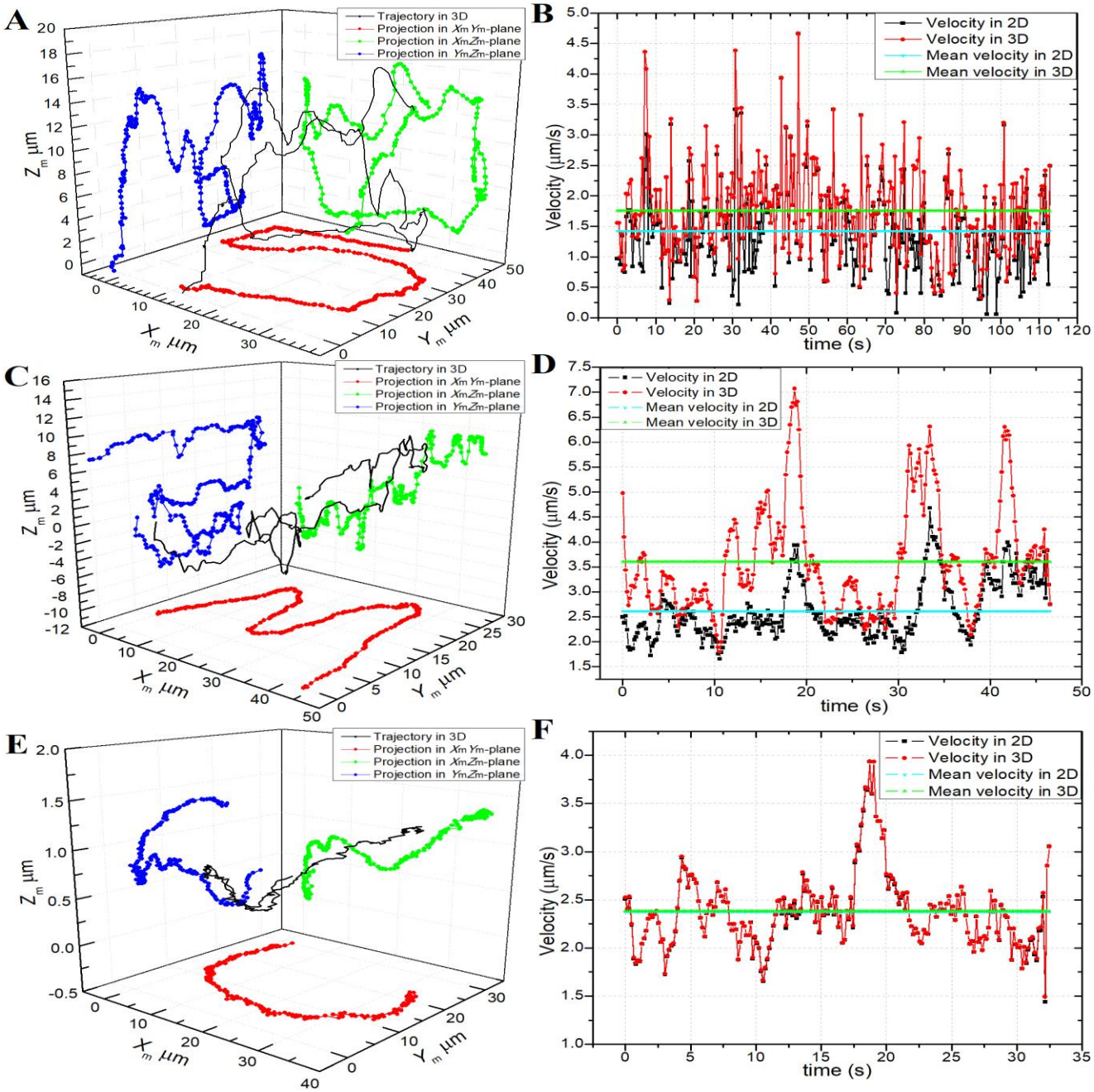

Figure 8. The trajectories of the nanorobots in 3D and velocity in 2D and 3D. (A-B) The 'S' trajectory, (C-D) the 'M' trajectory, and (E-F) the 'U' trajectory. Lines between points were added to guide the eye.

nanorobot in Figure 7B, which had a MH 5 × larger, decreased obviously when the rotating direction changed from counter-clockwise to clockwise, with the velocity difference incerasing as the rotation frequency increased. That means the larger sized MHs would decrease the velocity of the nanorobot more significantly when the nanorobot was moving backward from forward at the same rotating frequency. The sudden decrease in the velocities of Figure 7 at 20 Hz can be explained by the occurrence of a step-out frequency[52].

3D motion trajectories

Currently, most of the research focused on nanorobots is limited to 2D applications due to the difficulties in tracking the trajectories in Z_m direction through fluorescence microscopic imaging. In terms of control, 3D motion of nanorobots was achieved by manipulating the rotating magnetic field, which was generated from the magnetic field generator (c of Figure 2A). The rotating frequency could influence the speed of flagellar nanorobots linearly (see previous section) and at the same time the direction of the nanorobot could be manipulated by controlling the angles between the *z* axis of the nanorobot and the X_c, Y_c and Z_c axis respectively. The localization information in the X_mY_m plane was obtained in both the bright-fleld and fluorescence microscopy, however, the detection range under fluorescence microscopy visualization was limited in the Z_m direction (Movie S6). Thus, the Z_m direction displacement of flagellar nanorobot was tracked in the bright-field microscopy, which was dependent on the relationship between the distance from the focal plane to the MH and the size of the defocused MH in Figure 3B. Here, the flagellar nanorobots were navigated to swim in 3D, particularly the three projected trajectories having "S", "M" and "U" shapes at X_mY_m plane.

After recording the videos (Movie S7, actual experiment trajectories at X_mY_m plane are shown in Figure S6) MATLAB was used to recognize and record the trajectories of MH. The original videos were recorded at 15 frames per second (fps); to plot clear trajectories, the average locations of every 10, 5, and 5 frames were calculated and plotted respectively in three trajectories of "S", "M" and "U" in 3D. The trajectories in Figure 8A, C and E show the "S", "M" and "U" letters shaped trajectories in the bright-field. To clearly show the significant difference of the nanorobot in 3D motion, compared with 2D, the transient and mean velocities of the nanorobots in X_mY_m plane and $X_mY_mZ_m$ space are shown separately in Figure 8B, D and F. The velocities in 3D are visibly larger than the one shown in 2D, particularly when the Z_m direction velocity is large in both the "S" and "M" trajectories. On the other hand, in the "U" shaped trajectory, we set the γ (definition could be found in SI) close to 90 degrees, with the results in Figure 8E and F showing that the velocities in 2D and 3D are similar compared with the "S" and "M" trajectories.

Discussion

We reported a type of flexible nanorobot which was comprised of a helical bacterial flagellum and a magnetic nanoparticle. The helical tail was isolated from *Salmonella* typhimurium and used as experimental material to fabricate the smooth and burr-free flagella as the propeller. After biotinylating, the flagellum was attached to an avidin-magnetic nanoparticle which could be actuated using rotating magnetic fields. The whole fabrication process was cost-effective and suitable for bulk production, since billions of flagella can be produced during the isolation process. The results presented here demonstrate that these nanorobots can be visualized under fluorescence microscopy and bright-field microscopy, allowing for the performance of precise and controllable navigation in 3D within a conjugation buffer solution. These characteristics empower the nanorobot for use in potential applications of remote drug delivery in 3D, bio-environment mapping, and medical imaging, etc.

As suggested from literature [20], the helical shaped nano- and microswimmer has unique kinetic characteristics that make it ideal for *in vivo* and *in vitro* swimming. However, up to date, only a few experimental investigations about the relationship between geometry and the swimming behavior were performed. Here, the effects of swimming characteristics near the boundary, the frequency and direction of rotation, the length of the nanorobot, and the diameter of the MH were experimentally investigated. The results showed that the distance between the boundary and the nanorobot impacts the forward and lateral velocities of nanorobot, with less distance leading to higher forward and lateral velocity. The rotating frequency could linearly affect the velocity of the nanorobot. Longer flagella showed nonlinear increases to velocity, while decreasing MH size also demonstrated linearly improvements in velocity. Furthermore, the forward and backward velocities at clockwise and counter-clockwise were also shown to be different when the MH size varied; particularly, the backward velocity significantly decreased when the size of the MH was larger, compared with the forward velocity at same rotation frequency. Based on these relationships, optimal nanorobots could be chosen and designed for different applications. Using the relationship between the focal plane distance to the MH along Z_m direction, along with the defocused nanorobot size in the image, the displacement along the Z_m direction could be accurately calculated. Therefore, the navigation of flagellar nanorobots was extended from 2D to 3D, significantly improving the likelihood of nanorobots being used in biomedicine [53].

Conclusions

In this paper, the influences of the boundary, geometry size, and rotating frequency and direction on the kinetic characteristics of the flagellar nanorobot were investigated, and the 3D designed navigation and trajectory tracking were implemented. The fundamental kinetic characteristics in this paper are essential and critical for the future development of the applications of the helical nanorobot.

Experimental

Bacteria culture and flagellar harvesting.

The nanorobot was composed of a single flexible bacterial flagellum and a magnetic nanoparticle. The flagella were repolymerized from flagellin monomers that were harvested after the depolymerization of flagella from Salmonella typhimurium (SJW 1103). To cultivate enough S. typhimurium to produce large concentrations of flagella, a systematic culture and isolation procedure was used. First, 10 liters of the modified Luria-Bertani (LB) broth recipe (Table S1)) was used as a growth medium and placed inside an incubator (New Brunswick, Excella E25) at 36°C and shaken at 130 RPM for a 12-16 hours cultivation period (I of Figure 1B); bacteria were then isolated from the culture media by centrifuging at 3500 relative centrifugal force (rcf) for 35 minutes.

Fabrication of biotinylated flagella

The original flagella of *S. typhimurium* are unqualified for attaching to the magnetic nanoparticle head as they are sheared apart during the isolation process and are not chemically functionalized. The pelleted bacteria (II of Figure 1B) were then resuspended into a pH 6.5 polymerization buffer (Table S1). The flagella (III of Figure 1B) were sheared off from the bacterial bodies by shaking vigorously for at least 20 minutes; the flagella were then purified from the bacterial bodies by centrifuging for 15 minutes at 16,000 rcf, then the supernatant containing the flagella was transferred to a new centrifuge tube and diluted with polymerization buffer; then the flagella were purified from the residual culture media by centrifuging for 90 minutes at 100,000 rcf, thus the flagella were pelleted to the bottom of the centrifuge tubes, and the suspension, which contains the culture media, was discarded; after repeating the two purification processes 3 to 4 times, the purified flagella (IV of Figure 1B) were then resuspended in the polymerization buffer with a final volume of 2.0 ml. Then, 20% of the isolated flagella (V of Figure 1B) were taken and mixed with EZ-LinkTM NHS-Biotin (Thermo Scientific) for 30 minutes to be covered by biotin complex; both of the biotinylated flagella and unbiotinylated flagella solution were centrifuged at 16,000 rcf for 2 minutes to remove the bubbles inside. Both of them were then placed in a water bath at 65°C for 10 minutes to produce the biotinylated (VI of Figure 1B) and unbiotinylated (VII of Figure 1B) flagellin monomers; both solutions were then centrifuged at 150,000 rcf for one hour to remove any excess proteins or debris on the bottom. Based on the salting-out effect, the short flagella (seeds, longer than 200 nm, VIII of Figure 1B) could be obtained by introducing the biotinylated monomers into a 2 M sodium phosphate solution in a 1:1 volume ratio, for 60 minutes; the seeds (IX of Figure 1B) were then washed of sodium phosphate through being diluted twice and centrifuged at 100,000 rcf for one hour. The seeds were then introduced into the unbiotinylated monomers and uniformly mixed by vortexing for 30 seconds. The solution was then left to incubate for 48 hours at room temperature [54] to repolymerize the flagella (X of Figure 1B).

Fluorescence labeling and nanorobot assembling

Due to the flagella only having a 20 nm diameter, the biotinylated flagella are not visible under the fluorescence microscopy. To label the flagella with dye, the repolymerized flagella were gently resuspended using pH 7.5 conjugation buffer (Table S1) and centrifuged at 100,000 rcf for one hour; then, the pelleted flagella and Cy3 dye (GEPA23001, Sigma-Aldrich) were suspended by using conjugation buffer to 0.75 ml respectively, and were mixed for 2 hours, while 0.15 ml (5% the final volume) of 1 M $NaHCO_3$ was added to help the dye attach to the flagella. Currently, the repolymerized flagella were dyed, but fluorescent dyes and dyed seeds in the solution will reduce the imaging quality; therefore, the dyed flagella need to be centrifugated at 100,000 rcf for 1 hour, remove the supernate; then, the pelleted flagella were gently resuspended, and appropriately diluted with conjugation buffer. The dyed flagella (XI of Figure 1B) with one of their endpoints being biotinylated could be imaged by the fluorescence microscopy (Figure S4). Finally, the flagella (Figure S5) were introduced to the 290 nm diameter avidin covered superparamagnetic nanoparticles (Spherotech, SVM-025-5H). After 30 minutes, the nanorobots (XII of Figure 1B) were produced.

Sample preparation and imaging set up

The nanorobot was loaded into a circular polydimethylsiloxane (PDMS) chamber, approximately 4 mm in diameter and 1 mm in height, on top of a No. 1 coverslip, then the 18×18 mm^2 No. 1 coverslip was applied on top of the PDMS chamber in order to seal it, decrease the effect from outside airflow, and limit evaporation. The chamber was then loaded under the magnetic field generator situated on top of the inverted fluorescence microscope. A 100× oil emersion objective lens and an EMCCD camera recording at 15 frames per second (fps) were used to visualize and capture data from the experiments. The open-loop commercial software "daedalus" was applied to manage the power supply (ECB-820) and control the magnetic field generator (MFG-100, MagnebotiX); the magnetic power from the system rotated the nanorobot and could maneuver them in 3D space. To avoid overheating during the experiments, only 12 mT magnetic field was applied. The coordinate system of the magnetic control system is illustrated in the supplementary information (Figure 2B and C and Coordinates relationship in SI).

Conflicts of interest

There are no conflicts to declare.

Acknowledgements

Many thanks should be given to Dr. Seiji Kojima from Nagoya University for providing Salmonella typhimurium (SJW 1103), besides we gratefully acknowledge the help from Micah Oxner, Dr. Pia Vogel, and Dr. Jamel Ali.
This work was supported by the National Science Foundation (CBET#1827831, CMMI#1712096, and CMMI#1761060).

Notes and references

1 X. Yan, Q. Zhou, J. Yu, T. Xu, Y. Deng, T. Tang, Q. Feng, L. Bian, Y. Zhang, A. Ferreira and L. Zhang, *Advanced Functional Materials*, 2015, **25**, 5333-5342.

2 Y. Alapan, O. Yasa, O. Schauer, J. Giltinan, A.F.Tabak,V.Sourjikand M. Sitti, *Science Robotics*, 2018, **3**, eaar4423.

3 S. Ghosh and A. Ghosh, *Science Robotics*, 2018, **3**, eaaq0076.

4 S. Tottori, L. Zhang, F. Qiu, K. K. Krawczyk, A. Franco-Obregónand B. J. Nelson, *Advanced Materials*, 2012, **24**, 811-816.

5 H. Kim, U. K. Cheang, L. W. Rogowski and M. J. Kim, *Journal of Micro-Bio Robotics*, 2018, **14**, 41-49.

6 S. Schuerle, A. P. Soleimany, T. Yeh, G. M. Anand, M. Häberli,H.E. Fleming, N. Mirkhani, F. Qiu, S. Hauert, X. Wang, B.J.Nelsonand S. N. Bhatia, *Science Advances*, 2019, **5**, eaav4803.

7 A. Servant, F. Qiu, M. Mazza, K. Kostarelos and B. J. Nelson, *Advanced Materials*, 2015, **27**, 2981-2988.

8 X. Yan, Q. Zhou, M. Vincent, Y. Deng, J. Yu, J. Xu, T. Xu, T. Tang, L. Bian, Y.-X. J. Wang, K. Kostarelos and L. Zhang, *Science Robotics*, 2017, **2**, eaaq1155.

9 Y. Ding, F. Qiu, X. C. i. Solvas, F. W. Y. Chiu, B. J. Nelson and A. deMello, *Micromachines*, 2016, **7(2),25**.

10S. Erbas-Cakmak, D. A. Leigh, C. T. McTernan andA.L.Nussbaumer, *Chemical Reviews*, 2015, **115**, 10081-10206.

11 J. Ali, U. K. Cheang, J. D. Martindale, M. Jabbarzadeh,H.C.Fuand M. Jun Kim, *Scientific Reports*, 2017, **7**, 14098.

12K. Kim, X. Xu, J. Guo and D. L. Fan, *Nature Communications*, 2014, **5**, 3632.

13W. Wang, L. A. Castro, M. Hoyos and T. E. Mallouk, *ACSNano*,2012, **6**, 6122-6132.

14 S. Palagi, A. G. Mark, S. Y. Reigh, K. Melde, T. Qiu, H. Zeng, C. Parmeggiani, D. Martella, A. Sanchez-Castillo, N. Kapernaum,F. Giesselmann, D. S. Wiersma, E. Lauga and P. Fischer, *Nature Materials*, 2016, **15**, 647.

15 V. Magdanz, S. Sanchez and O. G. Schmidt, *Advanced Materials*, 2013, **25**, 6581-6588.

16W. F. Paxton, K. C. Kistler, C. C. Olmeda, A. Sen, S. K. St. Angelo, Y. Cao, T. E. Mallouk, P. E. Lammert and V. H. Crespi, *Journal of the American Chemical Society*, 2004, **126**, 13424-13431.

17 E. M. Purcell, *Proceedings of the National Academy of Sciences of the United States of America*, 1997, **94**, 11307-11311.

18 E. M. Purcell, *Am. J. Phys.*, 1977, **45**.

19J. J. Abbott, M. C. Lagomarsino, L. Zhang, L. Dong and B.J.Nelson, *Int. J. Rob. Res.*, 2009, **28**.

20 S. Palagi and P. Fischer, *Soft Rebotics*, 2018, **3**, 113-124.

21 O. G. Schmidt and K. Eberl, *Nature*, 2001, **410**, 168.

22 L. Zhang, J. J. Abbott, L. Dong, B. E. Kratochvil, D. Bell and B. J. Nelson, *Applied Physics Letters*, 2009, **94**, 064107.

23S. Schuerle, S. Pané, E. Pellicer, J. Sort, M. D. Baró and B.J.Nelson, *Small*, 2012, **8**, 1498-1502.

24 F. Qiu, R. Mhanna, L. Zhang, Y. Ding, K. Sugihara,M.Zenobi-Wong and B. J. Nelson, 2013.

25W. Gao, X. Feng, A. Pei, C. R. Kane, R. Tam, C. Hennessy and a. J. Wang, *Nano Letters*, 2014, **14**, 305-310.

26J. Ali, U. K. Cheang, A. Darvish, H. Kim and M. J. Kim, *APL Material*, 2017, **5**, 116106.

27 A. Ghosh and P. Fischer, *Nano Letters*, 2009, **9**, 2243-2245.

28 M. J. Brett and M. M. Hawkeye, *Science*, 2008, **319**, 1192-1193.

29 S. Venkataramanababu, G. Nair, P. Deshpande, J. M.A,S.Mohan and A. Ghosh, *Nanotechnology*, 2018, **29**, 255203.

30 R. M. Macnab, *Annual Review of Microbiology*, 2003, **57**, 77-100.

31 Y. M. N. D. Y. Bandara, J. Tang, J. Saharia, L. W. Rogowski,C.W.Ahn and M. Kim, *Analytical Chemistry*, 2019, **91**, 13665-13674.

32E. E. Keaveny, S. W. Walker and M. J. Shelley, *Nano Letters*, 2013, **13**, 531-537.

33 B. G. Hosu, K. r. Jakab, P. t. Ba´nki, F. I. To´th and G.Forgacs, *Review of Scientific Instruments*, 2003, **74**, 4158-4163.

34 X. Zhang, H. Kim and M. J. Kim, *IEEE Transactions on Instrumentation and Measurement*, 2019, **68**, 680-687.

35T. Li, S. Kheifets, D. Medellin and M. G. Raizen, *Science*,2010,**328**, 1673-1675.

36E. Donath, A. Krabi, M. Nirschl, V. M. Shilov, M. I. Zharkikhdand B. Vincent, *Journal of the Chemical Society, Faraday Transactions*, 1997, **93**, 115-119.

37 S. Schuerle, S. Erni, M. Flink, B. E. Kratochvil and B.J.Nelson, *IEEE Transactions on Magnetics*, 2013, **49**, 321-330.

38 H. C. Berg, *Annu. Rev. Biochem.*, 2003, **72**, 19-54.

39M. U. Daloglu, W. Luo, F. Shabbir, F. Lin, K. Kim, I. Lee, J.-Q. Jiang, W.-J. Cai, V. Ramesh, M.-Y. Yu and A. Ozcan, *Light: Science & Applications*, 2018, **7**, 17121.

40 M. U. Daloglu, F. Lin, B. Chong, D. Chien, M. Veli, W. Luo and A. Ozcan, *Scientific Reports*, 2018, **8**, 15650.

41 M. U. Daloglu and A. Ozcan, *Biology of Reproduction*, 2017, **97**, 182-188.

42M. Wu, J. W. Roberts and M. Buckley, *Experiments in Fluids*, 2005, **38**, 461-465.

43 M. P. Kummer, J. J. Abbott, B. E. Kratochvil, R. Borer, A. Senguland B. J. Nelson, *IEEE Transactions on Robotics*, 2010, **26**, 1006-1017.

44 L. Turner, W. S. Ryu and H. C. Berg, *Journal of Bacteriology*, 2000, **182**, 2793-2801.

45 S. Asakura and G. Eguchi, *Journal of Molecular Biology*, 1964, **10**, 42-56.

46 S. Asakura and T. Iino, *Journal of Molecular Biology*, 1972, **64**,251-256.

47 M. Wu, J. W. Roberts, S. Kim, D. L. Koch and M. P. DeLisa, *Applied and Environmental Microbiology*, 2006, **72**, 4987-4994.

48 S. K. Lai, Y.-Y. Wang, D. Wirtz and J. Hanes, *Advanced Drug Delivery Reviews*, 2009, **61**, 86-100.

49H. C. Fu, M. Jabbarzadeh and F. Meshkati, *Physical ReviewE*,2015, **91**, 043011.

50 C. Peters, O. Ergeneman, B. J. Nelson and C. Hierold, *IEEE 26th International Conference on Micro Electro Mechanical Systems (MEMS)*, 2013, **(IEEE, Piscataway, NJ, 2013)**, 564-567.

51L. W. Rogowski, M. Oxner, J. Tang and M. J. Kim, *Biomicrofluidics*, 2020, **14**, 024112.

52 A. W. Mahoney, N. D. Nelson, K. E. Peyer, B. J. Nelson and J. J. Abbott, *Applied Physics Letters*, 2014, **104**, 144101.

53J. Li, B. Esteban-Fernández de Ávila, W. Gao, L.Zhang and J.Wang, *Science Robotics*, 2017, **2**, eaam6431.

54 B. R. Gerber, S. Asakura and F. Oosawa, *Journal of Molecular Biology*, 1972, **774**, 467-487.